IR spectroscopic characterization of early 4d transition metal carbene cations, $ZrCH_2^+$ and $NbCH_2^+$

P. B. Armentrout,[1*] Olga V. Lushchikova,[2] Jelle L. Schuurman,[2] Sjoerd Nooteboom,[2] Maryam Ghiassee,[1] Georgia C. Boles,[1] and Joost M. Bakker[2]

[1]*University of Utah, Department of Chemistry, 315 South 1400 East, Salt Lake City, Utah 84112, United States*

[2]*Radboud University, Institute for Molecules and Materials, HFML-FELIX, Toernooiveld 7, 6525 ED Nijmegen, The Netherlands*

ABSTRACT

IR multiple-photon dissociation (IRMPD) action spectroscopy is combined with quantum chemical calculations to examine the $[M,C,2H]^+$ species for the early 4d metals, M = Zr and Nb. These ions were formed by reacting laser ablated M^+ ions with cyclopropane (*c*-C_3H_6) in a molecular beam apparatus. Both IRMPD spectra exhibit one major band near 700 cm^{-1} and a second weaker band at about twice that wavenumber, more evident when irradiated in focus. The $[Nb,C,2H]^+$ species also has a sharp band at 800 cm^{-1}. Comparison with B3LYP calculations allow assignment of the $[M,C,2H]^+$ structures to agostic carbenes, which is similar to the structures found for the 5d analogues, WCH_2^+ and $TaCH_2^+$. A molecular orbital analysis traces the reasons for the agostic deformation from a classic C_{2v} symmetric carbene.

*Corresponding author: armentrout@chem.utah.edu

INTRODUCTION

Although the activation and functionalization of C–H bonds has long been of interest,[1, 2] identification of catalysts that can initiate this reaction has been difficult. Ordinarily, because of the high C-H bond energies, the initial C-H bond activation step is the most difficult, with subsequent chemistry occurring more easily. In particular, because methane is a major component of natural gas, its activation is one of the best studied and technologically most important processes.[3-5] Early ion cyclotron resonance mass spectrometry (ICR-MS) experiments by Irikura and Beauchamp[6-8] and Freiser and co-workers[9] showed that several of the 5d (third-row) transition metal (TM) cations, Ta^+, W^+, Os^+, Ir^+, and Pt^+, react with methane at room temperature by dehydrogenation to form $[M,C,2H]^+$ products, as also confirmed by later studies.[10, 11] Guided ion beam tandem mass spectrometry (GIBMS) studies have determined the favorable energetics of these processes.[12-17] IR spectroscopic characterization of these $[M,C,2H]^+$ products showed that the early TM cations, Ta^+ and W^+, formed carbene structures distorted by agostic interactions.[18-20] In contrast, the later Os^+ and Ir^+ cations yielded hydrido metal carbyne $HMCH^+$ structures, although Ir^+ also exhibited experimental evidence for co-existence of a higher-energy symmetric $IrCH_2^+$ carbene structure.[18-21] Moving farther to the right, Pt^+ was shown to form a C_2v symmetric $PtCH_2^+$ carbene.[18-20] The agostic distortions shown by Ta and W occur because empty 5d orbitals on these metals accept electron density from one of the CH bonds. Because the late metals have no empty 5d orbitals, their carbenes are symmetric.

In contrast to third-row TM cations, the 3d (first-row) and 4d (second-row) TM cations do not react with methane at room temperature by dehydrogenation,[11, 22-35] except for Zr^+, where the reaction is quite inefficient.[36, 37] GIBMS experiments show that this inefficiency is because the reaction of methane with Zr^+ is slightly endothermic, by 0.13 ± 0.05 eV.[38] This is also consistent with the spectroscopic studies of Metz and co-workers,[39] who could obtain IR spectra of Ar tagged $Zr^+(CH_4)_{1,2}$ as well as $Zr^+(CH_4)_{3,4}$. Interestingly, they also provided evidence for seeing $(H_2)ZrCH_2^+(CH_4)_{0,1}$. Flow tube experiments have reported that reaction of Nb^+ with methane yields $NbCH_2^+$ (75%) and $Nb(CH_4)^+$ (25%) at thermal energies, albeit with an even lower overall

reaction efficiency than Zr^+, 0.4% of the collision rate.[11] ICR experiments found that this exothermic dehydrogenation process was associated with electronically excited Nb^+.[9] Once quenched, these ions do not react with methane at room temperature. This agrees with GIBMS experiments that show the reaction of ground state Nb^+ (^5D) with methane to form $NbCH_2^+ + H_2$ is endothermic by 0.30 ± 0.09 eV.[32]

Theory has shown that for both Zr^+ and Nb^+ in their ground electronic state, a methane adduct, $M^+(CH_4)$, is the only species that could be formed at thermal energies.[38-41] Also, in both cases, formation of ground state $MCH_2^+ + H_2$ requires changing spin. For Zr, the quartet spin surface of the Zr^+ (^4F) + CH_4 ($^1A_1$) ground state reactants shifts to the doublet spin surface of $ZrCH_2^+$ ($^2A'$) + H_2 ($^1\Sigma_g^+$) ground state products,[38] whereas the ground state for Nb^+ is ^5D and the ground state of $NbCH_2^+$ is ^3A.[32, 41] These theoretical calculations also indicate that the most likely position for the crossing point between spin surfaces lies in the entrance channel as the metal ion inserts into the CH bond to form a $H\text{-}M^+\text{-}CH_3$ intermediate having the same spin as the products. For Zr, this intermediate can evolve to ground state products along a doublet spin surface with no barriers in excess of the overall endothermicity. For Nb, the triplet spin surface has calculated barriers in excess of the overall endothermicity, but coupling to surfaces having singlet spin, which lead to a $H_2NbCH_2^+$ intermediate, and then back to the triplet spin state for the products conceivably provides a lower-energy, overall barrierless pathway.

To understand the periodic trends in the reactions with methane, it is of interest to characterize the structures of the putative $[M,C,2H]^+$ products for the 4d transition metal cations (TM^+). We recently used IR action spectroscopy to examine two of the late 4d TM^+s, Ru^+ and Rh^+, showing that the results were distinct from their Os^+ and Ir^+ congeners.[42] Whereas $[Os,C,2H]^+$ formed by reaction of Os^+ with methane was exclusively $HOsCH^+$, $[Ru,C,2H]^+$ formed by reaction of Ru^+ with oxirane (c-C_2H_4O) was a mixture of $HRuCH^+$ and a symmetric $RuCH_2^+$ carbene. $[Ir,C,2H]^+$ formed by reaction of Ir^+ with methane showed a mixture of both $IrCH_2^+$ and $HIrCH^+$, but $[Rh,C,2H]^+$ formed by reaction of Rh^+ with oxirane was found to be composed of two different

spin states of the symmetric $RhCH_2^+$ carbene. The two spin states led to extensive multiconfiguration character in the calculations needed to properly assign the experimental spectrum.

Here, we extend our studies of the 4d $[M,C,2H]^+$ species by examining two early TM^+ species, namely M = Zr and Nb. Previous GIBMS studies have shown that the reactions of these TM^+ with methane are endothermic. These studies have established that $D_0(Zr^+–CH_2)$ is 4.61 ± 0.05 eV[38, 43] and that $D_0(Nb^+–CH_2)$ is 4.44 ± 0.09 eV.[32] Given $D_0(CH_2–H_2)$ = 4.743 ± 0.001 eV,[44] the reactions of Zr^+ and Nb^+ with CH_4 are endothermic by 0.13 ± 0.05 and 0.30 ± 0.09 eV. Therefore, in order to form the $[M,C,2H]^+$ species of interest, we react the corresponding M^+ ions with cyclopropane (*c*-C_3H_6). Cyclopropane is reactive with many TM cations because of its ring strain and because $[M,C,2H]^+$ formation is accompanied by the stable C_2H_4 neutral product, such that extracting CH_2 requires much less energy, $D_0(CH_2–C_2H_4)$ = 3.948 ± 0.003 eV.[44] Thus, the reactions of M^+ with c-C_3H_6 to form $MCH_2^+ + C_2H_4$ are exothermic by 0.66 ± 0.05 and 0.49 ± 0.09 eV for M = Zr and Nb, respectively. Zr^+ has been shown to react with cyclopropane at thermal energies in GIBMS experiments to yield predominantly $ZrCH_2^+$ (19%), $ZrC_2H_2^+$ (12%), $ZrC_3H_2^+$ (20%), and $ZrC_3H_4^+$ (48%), with small amounts of $ZrC_2H_4^+$ (0.5%).[43] ICR-MS experiments found that the reaction of Nb^+ with c-C_3H_6 yields $NbCH_2^+$ (24%), $NbC_2H_2^+$ (11%), and $NbC_3H_2^+$ (65%).[9]

In the present work, we probe the structures of the $[M,C,2H]^+$ product ions for M = Zr and Nb using a combination of infrared multiple photon dissociation (IRMPD) action spectroscopy and density functional theory (DFT) calculations. IRMPD spectra were recorded using a molecular beam apparatus without mass-isolation prior to irradiation. Notably, for these four-atom systems, the sparsity of rovibrational states means that the intramolecular vibrational redistribution (IVR) is relatively slow, such that the enhanced power afforded by the intracavity configuration of the Free Electron Laser for Intra-Cavity Experiments (FELICE) is required. This has been demonstrated previously for $PtCH_2^+$, where extra-cavity photodissociation could not be observed.[45]

METHODS

Experimental

IRMPD action spectroscopy experiments on $[M,C,2H]^+$ systems were performed on the first beamline of FELICE using a molecular beam apparatus, as described in detail elsewhere.[46, 47] A solid metal target rod was rotated and translated within the molecular beam instrument. Atomic metal cations were formed in a laser ablation source[48, 49] by focusing the second harmonic of a pulsed Nd:YAG laser (532 nm) on the metal target. This created a plasma in a 3 mm diameter × 60 mm long channel that was collisionally cooled with helium injected into the channel via a pulsed valve (General Valve Series 9, stagnation pressure 5 bar). Cyclopropane (5 % in He, 0.5 bar stagnation pressure) was pulsed into the channel with a second pulsed valve approximately 50 mm downstream from the ablation source. Under the conditions used, 40-60% of the metal cations were found to react with cyclopropane. At the end of the reaction channel, the gas pulse expanded into vacuum and was shaped by a 2 mm diameter skimmer and a horizontal slit aperture (8 × 0.45 mm), both being electrically grounded. The molecular beam then entered the intracavity region and crossed the FELICE IR laser beam at an angle of 35°. FELICE is capable of producing IR radiation in the 100 – 2100 cm^{-1} spectral range but only the 250 – 1800 cm^{-1} range was used in the present study. The FELICE pulse train is a macropulse having a ~ 7 μs duration that consists of ps-long micropulses separated by 1 ns. The radiation was near transform-limited, and the spectral width was set to approximately 0.5% full width at half maximum (fwhm) of the central frequency (translating to about 5 cm^{-1} at 1000 cm^{-1}).

The molecular beam interacted with the FELICE IR light for a few μs before all ions were pulse extracted into a reflectron time-of-flight (RETOF) mass spectrometer (Jordan TOF Products, Inc.) with a mass resolution of $M/\Delta M \approx 1700$. Transients from the multichannel plate (MCP) detector were recorded with a 400 Msample/s 100 MHz digitizer (Acqiris DP310). The laser ablation and He/c-C_3H_6 gas pulses were run at twice the FELICE pulse rate. This allows the determination of fragments with and without the radiation provided by FELICE and permits collection of reference mass spectra to correct for long-term source fluctuations.

The experimental IRMPD spectra for $[M,C,2H]^+$ were constructed by calculating the fragmentation yield provided by $Y = -\ln[I_P/(I_P + I_F)]$ where I_F is the fragment ion intensity and I_P is the

precursor ion intensity. This fragment ion yield was corrected for the IR macropulse energy, as inferred from a fraction of the light coupled out of the cavity. During the experiments, the typical macropulse energies amounted to 0.6 – 0.8 J. In this work, the potential bare M^+ photodissociation product was not considered because, as noted above, a substantial amount of the bare metallic cation (40-60%) did not react, leaving it remaining in the molecular beam. Rather, the MC^+ fragments were considered exclusively.

Niobium is monoisotopic, ^{93}Nb, but the isotopic patterns of zirconium (51.5% ^{90}Zr, 11.2% ^{91}Zr, 17.1% ^{92}Zr, and 17.4% ^{94}Zr) can obscure some fragment ions. In both metal systems, previously measured thermochemistry indicates that the decomposition pathways observed require on the order of 3.0 eV for Zr and 2.5 eV for Nb, Table 1.[32, 38, 43] To achieve these decompositions, the minimum number of 600 cm^{-1} IR photons absorbed for M = Zr and Nb is 41 and 33 ± 2, respectively; whereas at 1600 cm^{-1}, only 15 and 13 ± 1 photons, respectively, are needed. Ordinarily, more photons than this minimum number are required in order for the rate of fragmentation to be sufficiently high for observation within the experimental time window, which is on the order of 10 – 20 μs.

The macropulse fluence in the experiment can be altered by translating the entire experimental apparatus along the FELICE laser beam. At a fixed wavenumber, the FELICE fluence can be reduced from the in-focus position by up to a factor of 30 at a maximum translation of 300 mm out of focus of the FELICE optical beam with its 55 mm Rayleigh range. As seen previously, the variation of the fluence leads to a relatively linear dependence of the fragmentation yield once a certain threshold has been overcome,[50, 51] until all ions in the interaction volume have fragmented and saturation leads to a broadening of spectral lines. As the strongest resonances can become saturated at IR fluences where smaller features are barely visible, spectra were recorded both at the maximum fluence (in-focus) and at a fixed translation of 240 mm from focus (out-of-focus). The spectra presented here were recorded with a compromise between suppression of broadening effects and the visibility of small resonances. The range of fluences in the in-focus position

extended from 25 J/cm^2 at 300 cm^{-1} to 150 J/cm^2 near 1400 cm^{-1}, with estimated peak power densities ranging from 4×10^8 to 1×10^{10} W/cm^2.

Computational

Using the Gaussian 16 software package,[52] molecular structures were optimized using the unrestricted B3LYP hybrid functional[53, 54] and the def2-TZVPPD basis set.[55] This triple-ζ basis set with dual polarization and diffuse functions uses a 28 electron (small core) effective core potential (ECP) on Zr and Nb, with the 4s, 4p, 5s, and 4d orbitals treated explicitly. All electrons were treated explicitly for H and C. This theoretical approach was used because the M^+–CH_2 bond dissociation energies calculated for the metals explored here matched the experimental values relatively well: $D_0(Zr^+–CH_2)$ = 4.37 eV (experimental 4.61 ± 0.05 eV) and $D_0(Nb^+–CH_2)$ = 4.40 eV (experimental 4.44 ± 0.09 eV). Relative energies provided here and below all include zero-point vibrational energy corrections with unscaled vibrational frequencies. We also performed single-point energy calculations at the coupled cluster with single, double, and perturbative triple excitations, CCSD(T), level utilizing the B3LYP geometries and zero-point corrections. These calculations indicate M^+-CH_2 bond dissociation energies of 4.20 and 4.19 eV, respectively, somewhat below the experimental values.

To ascertain true minima and for comparison with the experimental spectra, harmonic vibrational frequencies were calculated. For each vibrational mode, rovibrational envelopes were simulated assuming pure *a*-, *b*-, or *c*-type transitions and a rotational temperature of 100 K,[56] a temperature found to fit our previous spectral results for the $PtCH_2^+$ species better than room temperature.[57] The resulting rovibrational transition lines were then shifted to the harmonic vibrational frequencies that had been scaled by a factor of 0.95 to better match the observed band frequencies and convoluted with a Gaussian line shape function (FWHM = 0.9% of the central frequency), which mimics the FELICE spectral bandwidth. A similar scaling factor has previously been utilized for the WCH_2^+ spectrum.[19]

RESULTS & DISCUSSION

Reactions between M^+ (M = Zr and Nb) and cyclopropane resulted in the ionic products $[M,C,2H]^+$, $[M,2C,2H]^+$, $[M,3C,4H]^+$, $[M,4C,4H]^+$, $[M,5C,6H]^+$, and $[M,6C,8H]^+$, for both M, along with minor amounts of $[M,4C,6H]^+$, $[M,4C,8H]^+$, $[M,6C,6H]^+$, and $[M,9C,10H]^+$ for Nb. These product mass distributions are shown in Figure S1. The dominant product in both systems is dehydrogenation, which yields $[M,3C,4H]^+$.

$[Zr,C,2H]^+$

Zirconium has a complex isotopic distribution with natural abundances at 90 (51.5%), 91 (11.2%), 92 (17.1%), and 94 (17.4%) amu. Experimental thermochemistry (Table 1) indicates that dissociation of $ZrCH_2^+$ to yield $ZrC^+ + H_2$ requires 3.31 ± 0.16 eV and to form $ZrCH^+ + H$ requires 3.05 ± 0.14 eV, such that the two pathways are comparable in energy. Similarly, theory indicates that these two channels are nearly isoenergetic. Loss of CH_2 to form Zr^+ is much higher in energy at 4.61 ± 0.05 eV, as also found by theory. Because of the extensive overlap between the isotopes of Zr and ligation by C, CH, and CH_2, upon resonant IR irradiation, only two fragment masses at m/z = 102 and m/z = 103 can be clearly observed, Figure S1. The ratios of these two peaks suggest they are predominantly the $^{90}ZrC^+$ and $^{91}ZrC^+$ photofragments, although contributions of $^{90}ZrCH^+$ at m/z = 103 cannot be ruled out. The observation of both product channels is expected on the basis of the experimental thermochemistry, such that the preference for dehydrogenation observed here may suggest some revision in the literature thermochemistry for ZrC^+ or $ZrCH^+$ is needed.

Figure 1a shows the experimental IRMPD spectrum of $[Zr,C,2H]^+$. The spectrum was recorded using both out-of-focus and in-focus fluence conditions. It is constructed using only the ^{90}Zr isotope (*m/z* = 104) with ZrC^+ as the major photofragment observed (*m/z* = 102, Figure S2a). Here, a depletion of about 5% is observed out-of-focus. The spectrum of $[Zr,C,2H]^+$ in Figure 1a shows one dominant band peaking at 710 cm^{-1}, although the top of this band exhibits some structure. There is a much weaker, but very broad absorption at higher wavenumber that appears to have two maxima at ~1400 and 1550 cm^{-1}, as is visible in the enlarged spectrum. This broader structure

becomes more apparent when in focus, where the main band also broadens. A possible absorption at ~1000 cm^{-1} can also be seen in the in-focus spectrum.

As noted above, different $[Zr,C,2H]^+$ isomers and states were calculated at the B3LYP/def2-TZVPPD level along with single point energies at the CCSD(T) level using the same basis set and B3LYP geometries. Table 2 contains a complete listing of all stable $[Zr,C,2H]^+$ species located computationally. The $^2A'$ ground state (GS) is a distorted (agostic) zirconium carbene geometry. A low-lying electronic state, $^2A''$, has a similar geometry and is calculated to lie only 0.18 eV (0.22 eV at the CCSD(T) level) higher in energy. Increasing the spin state of the molecule leads to symmetric carbene structures (C_{2v} symmetry) with the lowest $^4B_2$ and $^4B_1$ states. These are calculated to lie 0.73 and 0.74 eV (0.90 and 0.90 eV at the CCSD(T) level) above the $^2A'$ GS.

The reason for the agostic distortion can be understood by comparing the molecular orbitals (MOs) of the C_{2v} and distorted structures, as shown in Figure 2. With the convention that the z-axis lies along the Zr-C bond and that the molecule lies in the yz plane, the (C_{2v}) $^4B_2$ state has two CH_2 bonding MOs ($1a_1$ and $1b_2$ symmetry, both double occupancy), a Zr–C σ bonding MO ($2a_1$, using mainly $4d_{z2}$ on Zr, double occupancy), a Zr–C π bond ($1b_1$, Zr $4d_{xz}$, single), and two non-bonding MOs localized on Zr: ($1a_2$, $4d_{xy}$, single) and ($4a_1$, largely 5s, single). Thus, the valence MO occupation (including the four CH_2 bonding electrons) is $(1a_1)^2(1b_2)^2(2a_1)^2(1b_1)^1(1a_2)^1(4a_1)^1$. The similar $^4B_1$ state shifts one of the non-bonding electrons from the $4d_{xy}$ ($1a_2$) MO to the $4d_{x2-y2}$ ($3a_1$), which explains the small energy difference between these two states. When the spin state is lowered, this enables one of the orbitals on Zr to be empty such that C-H bonding electrons can donate into this orbital, forming an "agostic" bond. This effect can be seen by noting that the distortion leads to the $1b_2$ MO (nearly pure CH_2 in character) gaining 4d character on Zr to become the 2a′ MO. Also, the 2a′ and 3a′ MOs essentially combine the $4d_{z2}$ and $4d_{yz}$ orbitals on Zr to enhance the bonding between Zr and CH_2. The remaining orbitals remain largely unchanged although the $1b_1$ gains $4d_{xz}$ character as it evolves to the 1a″ MO, and the $3a_1$ (pure $4d_{x2-y2}$) hybridizes with the 5s orbital as it forms the 4a′ MO. Thus, the electron configuration of the $^2A'$ GS is

$(1a')^2(2a')^2(3a')^2(1a'')^2(4a')^1$. The similar $^2A''$ state is formed by shifting the non-bonding 4a′ (5s-$4d_{x2-y2}$) electron to the 2a′′ ($4d_{xy}$) MO, explaining their similar energies.

In addition to these carbene structures, we also located hydrido zirconium carbyne states, $HZrCH^+$. The lowest of these is a $^2A'$ electronic state that lies 1.28 (1.33 for CCSD(T)) eV above the $^2A'$ carbene GS. Figure 2 shows the evolution of the MOs for this structure compared to the carbenes (C_s, C_{2v}). The (1a′, $1a_1$) MO remains a CH bonding orbital (1a′), whereas the CH_2 (2a′, $1b_2$) MO increases in energy and becomes the in-plane Zr-C π bond (4a′). The (3a′, $2a_1$) MO remains the Zr-C σ bond (2a′); and likewise, the (1a′′, $1b_1$) out-of-plane Zr-C π bond retains similar character in the 1a′′ MO of $HZrCH^+$. The 3a′ MO is the Zr-H σ bond and can be seen to evolve from the 4a′ MO of the C_s agostic structure, where the $4d_{x2-y2}$ orbital has hybridized with the Zr (5s) orbital. The next non-bonding $4d_{xy}$ MOs (2a′′, $1a_2$) evolve to the $HZrCH^+$ (2a′′) MO and acquire some out-of-plane Zr-C π bonding character. The (5a′, $4a_1$) MOs, largely Zr (5s), retains this character in the 5a′ MO of $HZrCH^+$. For the lowest energy $^2A'$ state of $HZrCH^+$, the valence MO occupation is $(1a')^2(2a')^2(3a')^2(1a'')^2(4a')^1$. In addition, there are $^2A''$, $^4A''$, and $^4A'$ states lying 1.53 (1.55), 2.07 (2.24), and 2.23 (2.35) eV above the carbene GS. In these states, a 1a′′ electron is moved to the 4a′, 5a′, or 2a′′ MO, respectively.

To examine the relationship between these various states and ensure that no low-lying states were missed, we also conducted relaxed potential energy surfaces scans at the B3LYP/def2-TZVPPD level. These are shown in Figure 3. At small ∠C-Zr-H bond angles, the difference between the agostic interactions of the doublet spin states (minima near 30°) and the C_{2v} symmetries of the quartet spin states (minima near 20°) is evident. As this bond angle increases, the surfaces evolve to the $HZrCH^+$ geometries with minima near 100°. Clearly, these hydrido carbyne structures are much higher in energy than the carbene-like structures. Along the $^2A''$ surfaces, there is a curve crossing that is probably avoided and occurs because of differing orbital occupations along the two surfaces.

Other possible structures, dihydrido zirconium carbides, H_2ZrC^+, or dihydrogen zirconium carbide, $(H_2)ZrC^+$, were also explored. Both $^4A''$ and $^2A''$ states of the former were located and lie

3.92 (3.96) and 4.47 (4.56) eV above the GS. For $(H_2)ZrC^+$ structures, $^2A'$ and $^4A''$ states were found at 2.62 (2.51) and 3.55 (3.54) eV above the GS, Table 2. Because the reaction of Zr^+ with cyclopropane is exothermic by 0.66 ± 0.05 eV, none of these alternative structures are expected to be formed easily in the present experiments.

Figure 1b-e shows simulated IR spectra of different $[Zr,C,2H]^+$ isomers and states calculated at the B3LYP level, with further isomers shown in Figure S3 of the Supporting Information. Table 3 includes the frequencies, intensities, and mode descriptions for all of these. The B3LYP IR spectrum for the $^2A'$ GS of $ZrCH_2^+$ (Figure 1b) is dominated by the CH_2 wag (a broad *c*-type transition) and Zr-C stretch (a narrow *a*-type transition) modes, which are calculated at 712 and 802 cm^{-1}, respectively. In Figure 1b, the vibrational spectrum has been scaled by 0.95, such that it now matches experiment quite well. The rotational band structure of this state could conceivably reproduce the fine structure seen in the experimental band. These vibrations are shifted to 658 and 793 cm^{-1} for the low-lying $^2A''$ state (Figure 1c), where they retain similar intensities but are somewhat broader. The CH_2 rock of both states (calculated at 513 and 462 cm^{-1}, respectively) is very weak in intensity and is a broad *b*-type transition. In contrast, the CH_2 scissors mode (a broad *b*-type transition), which lies near 1340 cm^{-1}, has appreciable intensity that is smeared out by the rotational band contours. Nevertheless, this mode does reproduce part of the broad band observed experimentally. As noted above, the formation of $ZrCH_2^+$ + ethene from reaction of Zr^+ with cyclopropane is exothermic by 0.66 ± 0.05 eV, such that only the $^2A'$ and $^2A''$ states should be formed easily. The predicted spectra for both species match the experimental spectrum rather well but are so similar that neither of them can explain the second band of the high-frequency broad structure around 1550 cm^{-1} or the band at 1000 cm^{-1} that becomes visible in the laser focus. One speculative assignment for the 1550 cm^{-1} band could be combination bands or overtones of the intense bands at 700 – 800 cm^{-1}. Another could be an electronic transition between the vibrationless ground states of the 2A' and 2A" states, that according to the current calculations would lie at 1460/1742 cm^{-1} using the B3LYP/CCSD(T) energies. Although unusual, electronic transitions have been observed previously in IRMPD spectra of M_5C_3[58] and cobalt clusters.[59] We have no obvious explanation for

the possible band at 1000 cm^{-1}. Despite these minor discrepancies, we assign the $[Zr,C,2H]^+$ species to the agostic zirconium carbene structures.

Figure 1d shows the spectrum for the symmetric $ZrCH_2^+$ ($^4B_2$) state. This exhibits peaks at 371 (CH_2 rock, a broad *b*-type transition), 607 (M-C stretch, a narrow *a*-type transition), and 687 (CH_2 wag, a broad *c*-type transition) cm^{-1}. The nearly isoenergetic $^4B_1$ state has a very similar spectrum (Figure S3) with peaks at 365, 606, and 686 cm^{-1}. For both states, the CH_2 scissors mode lies near 1326 cm^{-1} with very weak intensity (<1 km/mol). The sharp intense bands predicted at 606/607 cm^{-1} do not reproduce the experimental spectrum well. Likewise, the spectra for the hydrido zirconium carbyne cation in any state, Figures 1e and S3g - j, predict bands at lower wavenumber than the primary band observed at 710 cm^{-1} as well as an intense band near 1770 cm^{-1} (MH stretch) that has no experimental counterpart. We conclude that these higher energy alternative states and structures are unlikely to contribute to the experimental spectrum.

$NbCH_2^+$

Literature experimental thermochemistry indicates that dissociation of $NbCH_2^+$ to yield $NbC^+ + H_2$ requires 2.48 ± 0.17 eV and to form $NbCH^+ + H$ requires 2.75 ± 0.22 eV, such that the two pathways are comparable in energy, Table 1. Loss of CH_2 requires more energy, 4.44 ± 0.09 eV. Computational thermochemistry in this work places both lower-energy channels at near identical energies (Table 1). Upon photofragmentation of $[Nb,C,2H]^+$ (*m/z* = 107), NbC^+ (*m/z* = 105) was the only fragment observed, as shown in Figure S2b, consistent with the experimental thermochemistry mentioned above. The experimental IRMPD spectrum of $[Nb,C,2H]^+$ is shown in Figure 4a. Similar to the spectrum for the zirconium analogue, we observed a broad band peaking at 675 cm^{-1} again with some structure, along with a fairly sharp band at 800 cm^{-1}. In contrast to the $ZrCH_2^+$ spectrum, at lower fluences (out-of-focus), no extra structure appears, but at the higher fluence of the in-focus position, intensity at higher wavenumber (1000 – 1500 cm^{-1}) grows in, and the bands around 700 cm^{-1} broaden further.

Previous theoretical calculations for $[Nb,C,2H]^+$ at the CCSD(T)//MP2 (CCSD(T)//B3LYP) levels using the LANL2DZ basis on Nb and 6-311++G(d,p) basis on C and H identified a ^3A ground state, with ^5A and ^1A states lying 0.26 (0.24) and 0.46 (0.47) eV higher in energy, respectively.[41] Table 2 contains a complete listing of all stable $[Nb,C,2H]^+$ species located computationally in the present work. Our calculations find a $^3A''$ GS, which has the distorted, agostic carbene geometry and a valence MO occupation of $(1a')^2(2a')^2(3a')^2(1a'')^2(4a')^1(2a'')^1$. Low-lying $^3A'$ and $^1A'$ states move the non-bonding 2a″ ($4d_{xy}$) electron into either the non-bonding 5a′ (5s-like) or the 4a′ ($4d_{x2-y2}$) MO. These states lie 0.15 and 0.28 eV (0.14 and 0.22 eV at the CCSD(T) level) above the $^3A''$ GS. If the spin state is increased to quintet, then the molecule reverts to the symmetric C_{2v} carbene. $^5A_1$, $^5B_2$, and $^5A_2$ states were found at 0.89, 0.98, and 1.07 (0.98, 1.10, and 1.19 for CCSD(T)) eV about the GS. The valence configuration of the $^5A_1$ state is $(1a_1)^2(1b_2)^2(2a_1)^2(1b_1)^1(1a_2)^1(3a_1)^1(2b_2)^1$, where the $3a_1$ is now a 5s-$4d_{x2-y2}$ hybrid and the $2b_2$ MO is the antibonding analogue of the $1b_2$ bonding MO. For the $^5B_2$ state, the configuration is $(1a_1)^2(1b_2)^2(2a_1)^2(1b_1)^1(1a_2)^1(3a_1)^1(4a_1)^1(2b_2)^0$, and for the $^5A_2$ state, it is $(1a_1)^2(1b_2)^2(2a_1)^2(1b_1)^1(1a_2)^0(3a_1)^1(4a_1)^1(2b_2)^1$, where in both cases, the $3a_1$ and $4a_1$ MOs are now $4d_{x2-y2}$ and largely 5s, respectively.

As for the zirconium analogue, we also located hydrido niobium carbyne structures. The lowest of these is the $^1A'$ state lying 0.55 (0.42) eV above the $^3A''$ carbene GS. At higher energies, we located a $^3A'$ state, which lies 1.68 (1.72) eV above the GS, whereas the $^5A''$ state is 2.97 (3.19) eV higher in energy. These have valence MO occupations of $(1a')^2(2a')^2(3a')^2(1a'')^2(4a')^2$, $(1a')^2(2a')^2(3a')^2(1a'')^1(4a')^2(2a'')^1$, and $(1a')^2(2a')^2(3a')^2(1a'')^1(4a')^1(5a')^1(6a')^1$, respectively. Again to examine the relationship between the carbene and hydrido carbyne structures, we performed relaxed potential energy surfaces scans, as shown in Figure 5. Again the distinction between the agostic structures of the low-spin singlet and triplet states (minima near 35°) is evident by the larger ∠C-Nb-H bond angle compared to the quintet states that have C_{2v} symmetry (minima near 20°). As the bond angle increases, the surfaces evolve to yield the stable $HNbCH^+$ structures for $^1A'$ and $^5A''$ states. In contrast, on surfaces for the $^3A''$, $^3A'$, $^5A'$, and a second $^5A''$ state, there

is no minimum found for a $HNbCH^+$ geometry. Note that the $HNbCH^+$ minimum on the $^3A'$ surface connects to an excited state of a C_{2v} carbene, the $^3B_2$ state at 1.30 (1.34) eV above the GS.

We also searched for H_2NbC^+ structures (singlet, triplet, and quintet spin), but these all collapsed to either $HNbCH^+$ (singlet) or $NbCH_2^+$ structures. For $(H_2)NbC^+$ structures, $^1A'$, $^3A'$, $^3A''$ and $^5A'$ states were found 2.3 – 3.0 (2.0 – 3.2) eV above the GS, Table 2. Because the reaction of Nb^+ with cyclopropane is exothermic by 0.49 ± 0.09 eV, formation of singlet and triplet states of $NbCH_2^+$ and possibly the singlet state of $HNbCH^+$ is feasible experimentally.

Figure 4b-f shows the B3LYP simulated IR spectra of different $[Nb,C,2H]^+$ isomers and states, where again the calculated frequencies have been scaled by 0.95, with further isomers shown in Figure S4 of the Supporting Information. Table 4 includes the frequencies, intensities, and mode descriptions for all of these. The calculated IR spectra of the $^3A''$ GS and low-lying $^3A'$ and $^1A'$ states exhibit moderately intense bands with very similar frequencies (Figure 4b-d). These bands correspond to the Nb-C stretch (a narrow *a*-type transition, 24, 18, and 26 km/mol) near 850 cm^{-1} and CH_2 scissors (a broad *b*-type transition, 42, 47, and 41 km/mol) near 1385 cm^{-1}, and strong bands for the out-of-plane CH_2 wag (a broad *c*-type transition, 117, 111, and 122 km/mol) near 710 cm^{-1}, whereas the in-plane CH_2 rock modes (a broad *b*-type transition) near 600 cm^{-1} are relatively weak with intensities near 10 km/mol. The broader but more intense bands for the CH_2 wag agree well with the observed peak at 675 cm^{-1} and the experimental fine structure is possibly reproduced by the rotational band structure here (calculated at 100 K). The sharp band observed at 800 cm^{-1} likewise agrees fairly well with the predicted narrow Nb-C stretch bands. As noted above, the reaction of Nb^+ with cyclopropane to form $NbCH_2^+ + C_2H_4$ is exothermic by 0.49 ± 0.09 eV, such that formation of all three of these states is feasible experimentally. Therefore, we assign the experimental spectrum of $[Nb,C,2H]^+$ to the agostic carbene structures.

As noted above, the reaction with cyclopropane potentially has enough energy to form the $^1A'$ state of $HNbCH^+$, although the excitation energy of this state lies at the upper limit of the uncertainty in the exothermicity, Table 2. For this state, bands are predicted at 577 (broad *b*-type transition, 104 km/mol), 726 (broad *c*-type transition, 129 km/mol), 769 (broad *b*-type transition,

31 km/mol), and 999 (narrow *a*-type transition, 6 km/mol) cm^{-1}. As shown in Figure 4e, the spectrum for this structure is shifted to the red compared to the experimental spectrum and no longer has a sharp band that would reproduce the experimental band at 800 cm^{-1}. Figure 4f shows the spectrum of the lowest energy symmetric carbene structure, the $^5A_1$ state. It also is red shifted compared to the experiment and cannot easily explain the sharp 800 cm^{-1} band. We conclude that there is no evidence for the production of these higher energy structures under our experimental conditions.

Similar to the $ZrCH_2^+$ results, the CH_2 scissors bands near 1340 cm^{-1} might explain the very broad band observed at 1500 cm^{-1} under high fluence conditions of the in-focus position, Figure 4a-b. However, we also speculatively mention an electronic excitation here. The $ZrCH_2^+$ ($^3A'$) species is calculated at the CCSD(T) level to lie 0.136 eV above the $^3A''$ GS, with the $^1A_1$ state at 0.218 eV. These energies correspond to 1097 and 1758 cm^{-1}, which span the region of the experimental broad band.

CONCLUSION

Reacting the 4d group 5 and 6 transition metal cations, M^+ (M = Zr and Nb), with cyclopropane in a molecular beam source led to the formation of $[M,C,2H]^+$. These species were irradiated in the infrared intracavity free-electron laser FELICE, where they were spectroscopically characterized. The IRMPD spectra of both $[Zr,C,2H]^+$ and $[Nb,C,2H]^+$ are dominated by broad bands around 700 cm^{-1}, although $[Nb,C,2H]^+$ also has a sharp side band at 800 cm^{-1}. Both species exhibit some absorption at higher wavenumber (near 1400 cm^{-1}) when irradiated at maximum power. On the basis of B3LYP and CCSD(T)//B3LYP energetics, both species are expected to be distorted, agostic carbenes. Comparisons of the DFT calculated spectra for these species with the experimental IRMPD spectra offer good agreement once the broad rotational band structure of these species is properly included. These conclusions are consistent with previous conclusions regarding the early 5d congeners, $[W,C,2H]^+$ and $[Ta,C,2H]^+$.[18-20]

A detailed molecular orbital evaluation of the evolution between these agostic carbenes and symmetric C_{2v} carbenes demonstrates that empty d orbitals on the metal accept electron density from one of the C-H bonds, leading to the distortion. However, these species do not further evolve to the $HMCH^+$ hydrido carbyne structures. In the case of the zirconium complex, there are insufficient valence electrons needed to support the covalent Zr≡CH triple and Zr-H single bonds in this structure. For niobium, the singlet $^1A'$ state of $HNbCH^+$ does include all four covalent bonds (along with the C-H bond) and hence is low-lying, 0.55 (0.42) eV, but suffers from the loss of exchange energy associated with the higher spin states of the carbenes.

Supporting Information. Figures showing the mass spectrum for reaction between Zr^+ and Nb^+ with cyclopropane, the observed ion intensities of MCH_2^+ reactants and MC^+ products from IR irradiation, and additional comparisons between experimental and theoretical structures and states of $[Zr,C,2H]^+$ and $[Nb,C,2H]^+$.

ACKNOWLEDGMENTS

This work was funded by the National Science Foundation (grant no. CHE-2313553) and NWO's Materials for Sustainability program (grant no. 739.017.008). We gratefully acknowledge the Nederlandse Organisatie voor Wetenschappelijk Onderzoek (NWO) for the support of the FELIX Laboratory and the Center of High Performance Computing at the University of Utah for a generous grant of computer time.

REFERENCES

1. Crabtree, R. H. Organometallic alkane CH activation. *J. Organomet. Chem.* **2004,** *689*, 4083-4091.
2. Stone, K. L.; Borovik, A. S. Lessons from Nature: Unraveling Biological C–H Bond Activation. *Curr. Opin. Chem. Biol.* **2009,** *13*, 114–118.
3. Bohme, D. K.; Schwarz, H. Gas-Phase Catalysis by Atomic and Cluster Metal Ions: The Ultimate Single-Site Catalysts. *Angew. Chem. Int. Ed.* **2005,** *44*, 2336 – 2354.
4. Roithová, J.; Schröder, D. Selective Activation of Alkanes by Gas-Phase Metal Ions. *Chem. Rev.* **2010,** *110*, 1170–1211.

5. Sauer, J.; Freund, H. J. Models in Catalysis. *Catal. Lett.* **2015,** *145*, 109–125.
6. Irikura, K. K.; Beauchamp, J. L. Osmium Tetroxide and Its Fragment Ions in the Gas Phase: Reactivity with Hydrocarbons and Small Molecules. *J. Am. Chem. Soc.* **1989,** *111*, 75-85.
7. Irikura, K. K.; Beauchamp, J. L. Electronic Structure Considerations for Methane Activation by Third-row Transition-metal Ions. *J. Phys. Chem.* **1991,** *95*, 8344-8351.
8. Irikura, K. K.; Beauchamp, J. L. Methane Oligomerization in the Gas Phase by Third-Row Transition-Metal Ions. *J. Am. Chem. Soc.* **1991,** *113*, 2769-2770.
9. Buckner, S. W.; MacMahon, T. J.; Byrd, G. D.; Freiser, B. S. Gas-Phase Reactions of Nb^+ and Ta^+ with Alkanes and Alkenes. C-H Bond Activation and Ligand-Coupling Mechanisms. *Inorg. Chem.* **1989,** *28*, 3511-3518.
10. Achatz, U.; Beyer, M.; Joos, S.; Fox, B. S.; Niedner-Schatteburg, G.; Bondybey, V. E. The Platinum Hydrido-Methyl Complex: A Frozen Reaction Intermediate? *J. Phys. Chem. A* **1999,** *103*, 8200-8206.
11. Shayesteh, A.; Lavrov, V. V.; Koyanagi, G. K.; Bohme, D. K. Reactions of Atomic Cations with Methane: Gas Phase Room-Temperature Kinetics and Periodicities in Reactivity. *J. Phys. Chem. A* **2009,** *113*, 5602–5611.
12. Zhang, X.-G.; Liyanage, R.; Armentrout, P. B. The Potential Energy Surface for Activation of Methane by Pt^+: A Detailed Guided-Ion Beam Study. *J. Am. Chem. Soc.* **2001,** *123*, 5563-5575.
13. Armentrout, P. B.; Shin, S.; Liyanage, R. Guided-Ion Beam and Theoretical Study of the Potential Energy Surface for Activation of Methane by W^+ *J. Phys. Chem. A* **2006,** *110*, 1242-1260.
14. Li, F.-X.; Zhang, X.-G.; Armentrout, P. B. The Most Reactive Third-row Transition Metal: Guided Ion Beam and Theoretical Studies of the Activation of Methane by Ir^+. *Int. J. Mass Spectrom.* **2006,** *255/256*, 279-300.
15. Parke, L. G.; Hinton, C. S.; Armentrout, P. B. Experimental and Theoretical Studies of the Activation of Methane by Ta^+ and the Bond Energies of Ta^+-CH_x (x = 1 - 3). *J. Phys. Chem. C* **2007,** *111*, 17773-17787.
16. Armentrout, P. B.; Parke, L.; Hinton, C.; Citir, M. Activation of Methane by Os^+: Guided Ion Beam and Theoretical Studies. *ChemPlusChem* **2013,** *78*, 1157-1173.
17. Armentrout, P. B. Methane Activation by 5d Transition Metals: Energetics, Mechanisms, and Periodic Trends. *Chem.: Eur. J.* **2017,** *23*, 10-18.
18. Lapoutre, V. J. F.; Redlich, B.; van der Meer, A. F. G.; Oomens, J.; Bakker, J. M.; Sweeney, A.; Mookherjee, A.; Armentrout, P. B. Structures of the Dehydrogenation Products of Methane Activation by 5d Transition Metal Cations. *J. Phys Chem. A* **2013,** *117*, 4115-4126.
19. Owen, C. J.; Boles, G. C.; Chernyy, V.; Bakker, J. M.; Armentrout, P. B. Structures of the Dehydrogenation Products of Methane Activation by 5d Transition Metal Cations Revisited: Deuterium Labeling and Rotational Contours. *J. Chem. Phys.* **2018,** *148*, 044307.
20. Bakker, J. M.; Owen, C. J.; Nooteboom, S. W.; Lushchikova, O. V.; Armentrout, P. B. Structural characterization of $[M,C,2H]^+$ products formed by reaction of 5d metal cations Pt^+ and Ir^+ with ethylene oxide and Ta^+ with methane using messenger spectroscopy. *J. Mol. Spectrosc.* **2021,** *378*, 111472.
21. Armentrout, P. B.; Kuijpers, S.; Lushchikova, O.; Hightower, R. L.; Boles, G. C.; Bakker, J. M. Spectroscopic Identification of the Carbyne Hydride Structure of the Dehydrogenation Product of Methane Activation by Osmium Cations. *J. Am. Soc. Mass Spectrom.* **2018,** *29*, 1781-1791.

22. Halle, L. F.; Armentrout, P. B.; Beauchamp, J. L. Formation of Chromium Carbene Ions by Reaction of Electronically Excited Chromium Ions with Methane in the Gas Phase. *J. Am. Chem. Soc.* **1981,** *103*, 962-963.
23. Aristov, N.; Armentrout, P. B. Methane Activation by V^+: Electronic and Translational Energy Dependence. *J. Phys. Chem.* **1987,** *91*, 6178-6188.
24. Schultz, R. H.; Elkind, J. L.; Armentrout, P. B. Electronic Effects in C-H and C-C Bond Activation: State-specific Reactions of $Fe^+(^6D, ^4F)$ with Methane, Ethane and Propane. *J. Am. Chem. Soc.* **1988,** *110*, 411-423.
25. Sunderlin, L. S.; Armentrout, P. B. Methane Activation by Ti^+: Electronic and Translational Energy Dependence. *J. Phys. Chem.* **1988,** *92*, 1209-1219.
26. Georgiadis, R.; Armentrout, P. B. Translational and Electronic Energy Dependence of Chromium Ion Reactions with Methane. *J. Phys. Chem.* **1988,** *92*, 7067-7074.
27. Sunderlin, L. S.; Armentrout, P. B. Periodic Trends in Chemical Reactivity: Reactions of Sc^+, Y^+, La^+, and Lu^+ with Methane and Ethane. *J. Am. Chem. Soc.* **1989,** *111*, 3845-3855.
28. Georgiadis, R.; Armentrout, P. B. Translational and Electronic Energy Dependence of the Reaction of Mn^+ with Ethane. *Int. J. Mass Spectrom. Ion Process.* **1989,** *91*, 123-133.
29. Haynes, C. L.; Chen, Y.-M.; Armentrout, P. B. The Potential Energy Surface for Activation of Methane by Co^+: An Experimental Study. *J. Phys. Chem.* **1995,** *99*, 9110-9117.
30. Chen, Y.-M.; Armentrout, P. B. Activation of Methane by Gas-Phase Rh^+. *J. Phys. Chem.* **1995,** *99*, 10775-10779.
31. Chen, Y.-M.; Sievers, M. R.; Armentrout, P. B. Activation of CH_4, C_2H_6, C_3H_8, and c-C_3H_6 by Gas-phase Pd^+ and the Thermochemistry of Pd-ligand Complexes. *Int. J. Mass Spectrom. Ion Processes* **1997,** *167/168*, 195-212.
32. Sievers, M. R.; Chen, Y.-M.; Haynes, C. L.; Armentrout, P. B. Activation of CH_4, C_2H_6, and C_3H_8 by Gas-Phase Nb^+ and the Thermochemistry of Nb-ligand Complexes. *Int. J. Mass Spectrom.* **2000,** *195/196*, 149-170.
33. Liu, F.; Zhang, X.-G.; Armentrout, P. B. Activation of CH_4 by Gas-phase Ni^+ and the Thermochemistry of Ni Ligand Complexes. *Phys. Chem. Chem. Phys.* **2005,** *7*, 1054-1064.
34. Armentrout, P. B. Activation of CH_4 by Gas-phase Mo^+ and the Thermochemistry of Mo-ligand Complexes. *J. Phys. Chem. A* **2006,** *110*, 8327-8338.
35. Armentrout, P. B.; Chen, Y.-M. Activation of Methane by Ru^+: Experimental and Theoretical Studies of the Thermochemistry and Mechanism. *Int. J. Mass Spectrom.* **2016,** *413*, 135-149.
36. Ranasinghe, Y. A.; MacMahon, T. J.; Freiser, B. S. Formation of Thermodynamically Stable Dications in the Gas Phase by Thermal Ion-Molecule Reactions: Ta^{2+} and Zr^{2+} with Small Alkanes. *J. Phys. Chem* **1991,** *95*, 7721-7726.
37. Van Koppen, P. A. M.; Kemper, P. R.; Bushnell, J. E.; Bowers, M. T. Methane Dehydrogenation by Ti^+: A Cluster-Assisted Mechanism for σ-Bond Activation. *J. Am. Chem. Soc.* **1995,** *117*, 2098-2099.
38. Armentrout, P. B.; Sievers, M. R. Activation of CH_4 by Gas-phase Zr^+ and the Thermochemistry of Zr ligand Complexes. *J. Phys. Chem. A* **2003,** *107*, 4396-4406.
39. Kozubal, J.; Heck, T.; Metz, R. B. Vibrational Spectroscopy of Intermediates and C–H Activation Products of Sequential Zr^+ Reactions with CH_4. *J. Phys. Chem. A* **2020,** *124*, 8235-8245.
40. Blomberg, M. R. A.; Siegbahn, P. E. M.; Svensson, M. Reaction of Second-Row Transition-Metal Cations with Methane. *J. Phys. Chem.* **1994,** *98*, 2062-2071.

41. de Almeida, K. J.; Ramalho, T. C.; Neto, J. L.; Santiago, R. T.; Felicíssimo, V. C.; Duarte, H. A. Methane Dehydrogenation by Niobium Ions: A First-Principles Study of the Gas-Phase Catalytic Reactions. *Organomet.* **2013,** *32*, 989-999.
42. Wensink, F. J.; Smink, C. E.; Stevenson, B. C.; Steele, R. P.; Armentrout, P. B.; Bakker, J. M. IR spectroscopic characterization of $[M,C,2H]^+$ (M = Ru and Rh) products formed by reacting 4d transition metal cations with oxirane: Spectroscopic evidence for multireference character in $RhCH_2^+$. *Phys. Chem. Chem. Phys.* **2024**, submitted for publication.
43. Sievers, M. R.; Armentrout, P. B. Activation of C_2H_6, C_3H_8, and c-C_3H_6 by Gas-phase Zr^+ and the Thermochemistry of Zr-ligand Complexes. *Organomet.* **2003,** *22*, 2599-2611.
44. Ruscic, B.; Bross, D. H. Active Thermochemical Tables (ATcT) values based on ver. 1.130 of the Thermochemical Network. available at ATcT.anl.gov (accessed 2/12/24).
45. Wheeler, O. W.; Salem, M.; Gao, A.; Bakker, J. M.; Armentrout, P. B. Activation of C-H bonds in $Pt^+ + xCH_4$ Reactions, Where x = 1 – 4: Identification of the Platinum Dimethyl Cation. *J. Phys. Chem. A* **2016,** *120*, 6216–6227.
46. Bakker, J. M.; Lapoutre, V. J. F.; Redlich, B.; Oomens, J.; Sartakov, B. G.; Fielicke, A.; von Helden, G.; Meijer, G.; van der Meer, A. F. G. Intensity-resolved IR Multiple Photon Ionization and Fragmentation of C_{60}. *J. Chem. Phys.* **2010,** *132*, 074305.
47. Oomens, J.; Sartakov, B. G.; Meijer, G.; von Helden, G. Gas-phase Infrared Multiple Photon Dissociation Spectroscopy of Mass-selected Molecular Ions. *Int. J. Mass Spectrom.* **2006,** *254*, 1-19.
48. Dietz, T. G.; Duncan, M. A.; Powers, D. E.; Smalley, R. E. Laser Production of Supersonic Metal Cluster Beams. *J. Chem. Phys.* **1981,** *74*, 6511-6512.
49. Haertelt, M.; Lapoutre, V. J. F.; Bakker, J. M.; Redlich, B.; Fielicke, A.; Meijer, G. Structure Determination of Anionic Metal Clusters via Infrared Resonance Enhanced Multiple Photon Electron Detachment Spectroscopy. *J. Phys. Chem. Lett.* **2011,** *2*, 1720-1724.
50. Simon, A.; MacAleese, L.; Maître, P.; Lemaire, J.; McMahon, T. B. Fingerprint Vibrational Spectra of Protonated Methyl Esters of Amino Acids in the Gas Phase. *J. Am. Chem. Soc.* **2007,** *129*, 2829-2840.
51. Bakker, J. M.; Besson, T.; Lemaire, J.; Scuderi, D.; Maître, P. Gas-Phase Structure of a π-allyl-Palladium Complex: Efficient Infrared Spectroscopy in a 7T Fourier Transform Mass Spectrometer. *J. Phys. Chem. A* **2007,** *111*, 13415-13424.
52. Frisch, M. J.; Trucks, G. W.; Schlegel, H. B.; Scuseria, G. E.; Robb, M. A.; Cheeseman, J. R.; Scalmani, G.; Barone, V.; Petersson, G. A.; Nakatsuji, H., et al. *Gaussian 16 Rev. C.01*, Wallingford, CT, 2016.
53. Becke, A. D. Density-functional Thermochemistry. III. The Role of Exact Exchange. *J. Chem. Phys.* **1993,** *98*, 5648-5652.
54. Lee, C.; Yang, W.; Parr, R. G. Development of the Colle-Salvetti Correlation-Energy Formula into a Functional of the Electron Density. *Phys. Rev. B* **1988,** *37*, 785-789.
55. Rappoport, D.; Furche, F. Property-Optimized Gaussian Basis Sets for Molecular Response Calculations. *J. Chem. Phys.* **2010,** *133*, 134105.
56. Meerts, W. L.; Schmitt, M. Application of Genetic Algorithms in Automated Assignments of High-Resolution Spectra. *Int. Rev. Phys. Chem.* **2006,** *25*, 353-406.
57. Wensink, F. J.; Roos, N.; Bakker, J. M.; Armentrout, P. B. C–H Bond Activation and C–C Coupling of Methane on a Single Cationic Platinum Center: A Spectroscopic and Theoretical Study. *Inorg. Chem.* **2022,** *61*, 11252-11260.

58. Chernyy, V.; Logemann, R.; Kirilyuk, A.; Bakker, J. M. Direct IR Spectroscopic Detection of a Low-Lying Electronic State in a Metal Carbide Cluster. *ChemPhysChem* **2018,** *19*, 1424-1427.
59. Kaw, K. A.; Louwerse, R. J.; Bakker, J. M.; Lievens, P.; Janssens, E.; Ferrari, P. Direct probing of low-energy intra d-band transitions in gas-phase cobalt clusters. *Communications Chemistry* **2024,** *7*, 124.

Table 1: Fragmentation channels and dissociation energies (D_0) of the lowest energy $[M,C,2H]^+$ species.

Species	Fragments	Bond dissociation energy D_0 (eV)		
		B3LYP [a]	CCSD(T) [a]	Experiment
$ZrCH_2^+$	$Zr^+ + CH_2$	4.37	4.20	4.61 ± 0.05 [b]
	$ZrC^+ + H_2$	3.17	2.97	3.31 ± 0.16 [b,c]
	$ZrCH^+ + H$	3.24	2.98	3.05 ± 0.14 [b,c]
$NbCH_2^+$	$Nb^+ + CH_2$	4.40	4.19	4.44 ± 0.09 [d]
	$NbC^+ + H_2$	3.01	2.74	2.48 ± 0.17 [c,d]
	$NbCH^+ + H$	3.00	2.76	2.75 ± 0.22 [c,d]

[a] Theoretical values are calculated at the level of theory shown using the def2-TZVPPD basis set and B3LYP geometries and zero point corrections. [b] Refs. [43]. [c] Uses $D_0(C–H_2)$ = 3.320 ± 0.001 eV or D_0(CH-H) = 4.330 ± 0.001 eV.[44] [d] Ref. [32].

Table 2: Ground and excited electronic states for $[M,C,2H]^+$ isomers with electronic occupation for selected states calculated at the B3LYP/def2-TZVPPD level. The relative energy at 0 K, E_{rel}, is given with respect to the lowest energy isomer for the metal involved.

Species	State	E_{rel} (eV)		Valence MO Occupation
		B3LYP[a]	CCSD(T)[a]	
$ZrCH_2^+$	$^2A'$	0.000	0.000	$(1a')^2(2a')^2(3a')^2(1a'')^2(4a')^1$
	$^2A''$	0.181	0.216	$(1a')^2(2a')^2(3a')^2(1a'')^2(2a'')^1$
	$^4B_2$	0.732	0.902	$(1a_1)^2(1b_2)^2(2a_1)^2(1b_1)^1(1a_2)^1(4a_1)^1$
	$^4B_1$	0.735	0.902	$(1a_1)^2(1b_2)^2(2a_1)^2(1b_1)^1(3a_1)^1(4a_1)^1$
	$^2B_1$	0.968	1.134	$(1a_1)^2(1b_2)^2(2a_1)^2(1b_1)^1(3a_1)^1(4a_1)^1$
$HZrCH^+$	$^2A'$	1.284	1.329	$(1a')^2(2a')^2(3a')^2(1a'')^2(4a')^1$
	$^2A''$	1.534	1.550	$(1a')^2(2a')^2(3a')^2(1a'')^1(4a')^2$
	$^4A''$	2.067	2.236	$(1a')^2(2a')^2(3a')^2(1a'')^1(4a')^1(5a')^1$
	$^4A'$	2.233	2.349	$(1a')^2(2a')^2(3a')^2(1a'')^1(4a')^1(2a'')^1$
$(H_2)ZrC^+$	$^2A'$	2.624	2.507	
	$^4A''$	3.550	3.536	
H_2ZrC^+	$^4A''$	3.919	3.962	
	$^2A''$	4.467	4.556	
$NbCH_2^+$	$^3A''$	0.000	0.000	$(1a')^2(2a')^2(3a')^2(1a'')^2(4a')^1(2a'')^1$
	$^3A'$	0.151	0.136	$(1a')^2(2a')^2(3a')^2(1a'')^2(4a')^1(5a')^1$
	$^1A'$	0.284	0.218	$(1a')^2(2a')^2(3a')^2(1a'')^2(4a')^2$
	$^5A_1$	0.894	0.976	$(1a_1)^2(1b_2)^2(2a_1)^2(1b_1)^1(1a_2)^1(3a_1)^1(2b_2)^1$
	$^5B_2$	0.982	1.096	$(1a_1)^2(1b_2)^2(2a_1)^2(1b_1)^1(1a_2)^1(3a_1)^1(4a_1)^1$
	$^5A_2$	1.068	1.193	$(1a_1)^2(1b_2)^2(2a_1)^1(1b_1)^1(3a_1)^1(4a_1)^1(2b_2)^1$
	$^3B_2$	1.299	1.387	$(1a_1)^2(1b_2)^2(2a_1)^2(1b_1)^1(1a_2)^1(3a_1)^2$
	$^5A_2$	1.804	1.813	$(1a_1)^2(1b_2)^2(2a_1)^2(1b_1)^1(1a_2)^1(3a_1)^1(2b_1)^1$

$HNbCH^+$	$^1A'$	0.548	0.423	$(1a')^2(2a')^2(3a')^2(1a'')^2(4a')^2$
	$^3A'$	1.683	1.716	$(1a')^2(2a')^2(3a')^2(1a'')^1(4a')^2(2a'')^1$
	$^5A''$	2.970	3.193	$(1a')^2(2a')^2(3a')^2(1a'')^1(4a')^1(5a')^1(6a')^1$
$(H_2)NbC^+$	$^3A''$	2.337	2.116	
	$^1A'$	2.368	2.021	
	$^3A'$	2.626	2.444	
	$^5A'$	2.970	3.193	

[a] Theoretical values are calculated at the level of theory shown using the def2-TZVPPD basis set and B3LYP geometries and zero point corrections.

Table 3: Experimental band positions and strengths (s=strong, m=medium, w=weak) accompanied by theoretical calculated frequencies, intensities, and descriptions for the assigned structures.

Structure (state)	Experiment		Theory B3LYP[a]		
	Frequency (cm^{-1})	Strength	Frequency (cm^{-1})	Intensity (km/mol)	Mode description (type)
$ZrCH_2^+$ ($^2A'/^2A''$)			513 / 462	3 / 4	CH_2 rock (b)
	710	s	712 / 658	143 / 135	CH_2 wag (c)
			802 / 793	47 / 32	M–C stretch (a)
	1400	w	1354 / 1325	44 / 45	CH_2 scissor (b)
			2672 / 2788	16 / 12	agostic C–H str.
			3192 / 3191	50 / 31	free C–H stretch
$ZrCH_2^+$ ($^4B_2/^4B_1$)			371 / 365	9 / 8	CH_2 rock (b)
			607 / 606	33 / 34	M–C stretch (a)
	710	s	687 / 686	45 / 45	CH_2 wag (c)
	1400	w	1327 / 1325	1 / 1	CH_2 scissor (b)
			3056 / 3056	36 /36	sym C–H stretch
			3142 / 3141	6 / 5	asym C–H stretch
$HZrCH^+$ ($^2A'/^2A''$)			326 / 521	59 / 140	HM ip bend (a)
	710	s	572 / 663	40 / 41	C–H ip bend (b)
			665 / 591	150 / 61	CH oop bend (c)
	1400	w	832 / 842	17 / 25	M–C stretch (a)
			1769 / 1776	145 / 138	M–H stretch (b)
			3162 / 3163	45 / 48	C–H stretch

[a] When two values appear, these correspond to the two electronic states specified in the first column.

Table 4: Experimental band positions and strengths (s=strong, m=medium, w=weak) accompanied by theoretical calculated frequencies, intensities, and descriptions for the assigned structures.

Structure (state)	Experiment		Theory B3LYP[a]		
	Frequency (cm^{-1})	Strength	Frequency (cm^{-1})	Intensity (km/mol)	Mode description (type)
$NbCH_2^+$ ($^3A''/^3A'$)			581 / 639	6 / 13	CH_2 rock (b)
	675	s	708 / 720	117 / 111	CH_2 wag (c)
	800	m	837 / 857	24 / 18	M–C stretch (a)
	1400	w	1384 / 1389	42 / 47	CH_2 scissor (b)
			2561 / 2534	11 / 6	agostic C–H str.
			3193 / 3186	63 / 54	free C–H stretch
$NbCH_2^+$ ($^1A'$)			575	4	CH_2 rock (b)
	675	s	708	122	CH_2 wag (c)
	800	m	852	26	M–C stretch (a)
	1400	w	1384	41	CH_2 scissor (b)
			2578	14	agostic C–H str.
			3193	68	free C–H stretch
$HNbCH^+$ ($^1A'$)			577	104	HM ip bend (b)
	675	s	726	129	C–H oop bend (c)
	800	m	769	31	CH ip bend (b)
	1400	w	999	6	M–C stretch (a)
			1903	71	M–H stretch
			3159	61	C–H stretch

[a] When two values appear, these correspond to the two electronic states specified in the first column.

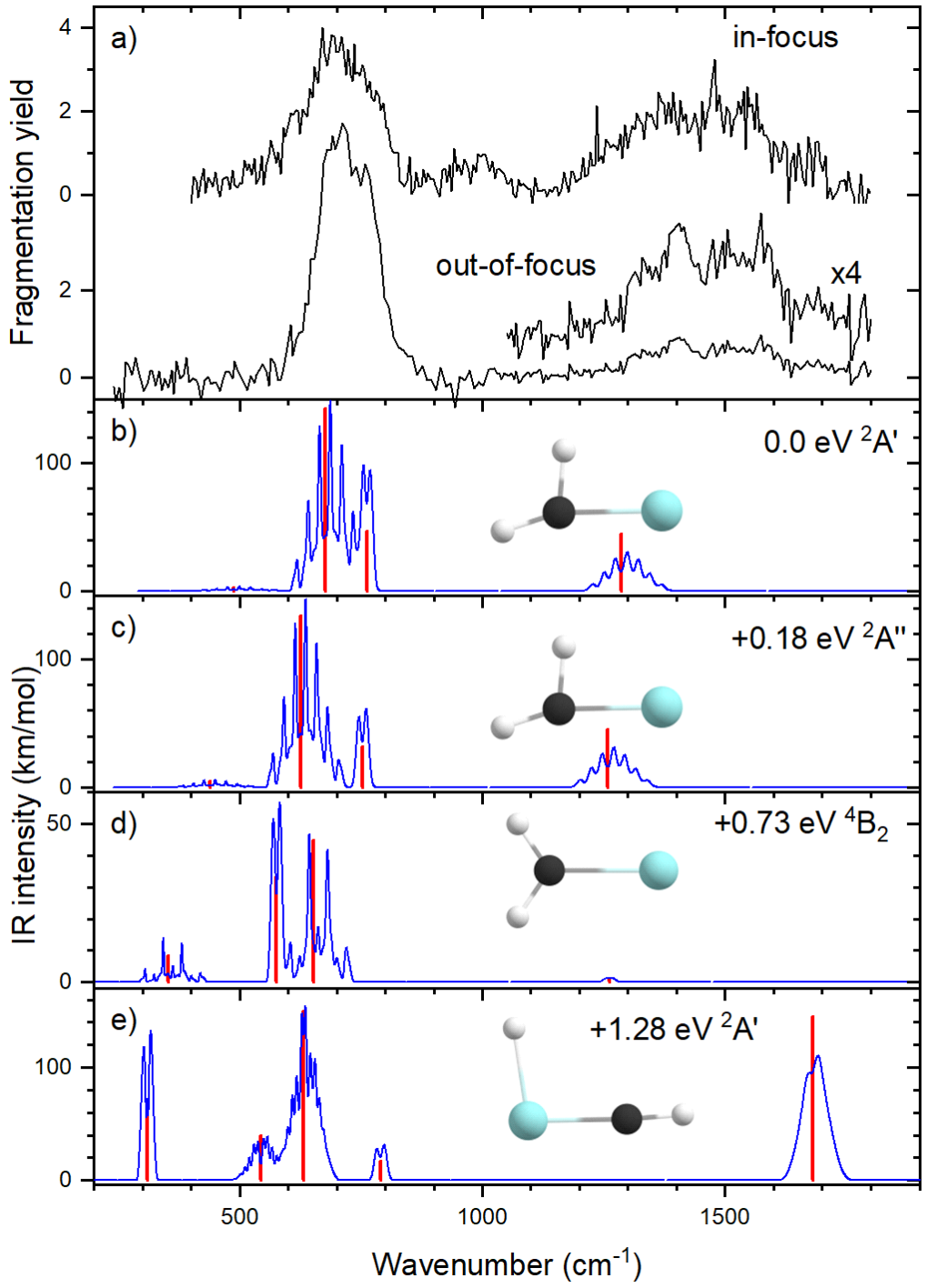

Figure 1: (a) Experimental IRMPD spectrum of $[Zr,C,2H]^+$; b-d) B3LYP/def2-TZVPPD calculated IR spectra of different $[Zr,C,2H]^+$ states and isomers with the harmonic vibrations in red and the rovibrational envelopes (calculated at 100 K) in blue accompanied by geometric structure, relative energy, and electronic state. Theoretical frequencies are scaled by 0.95.

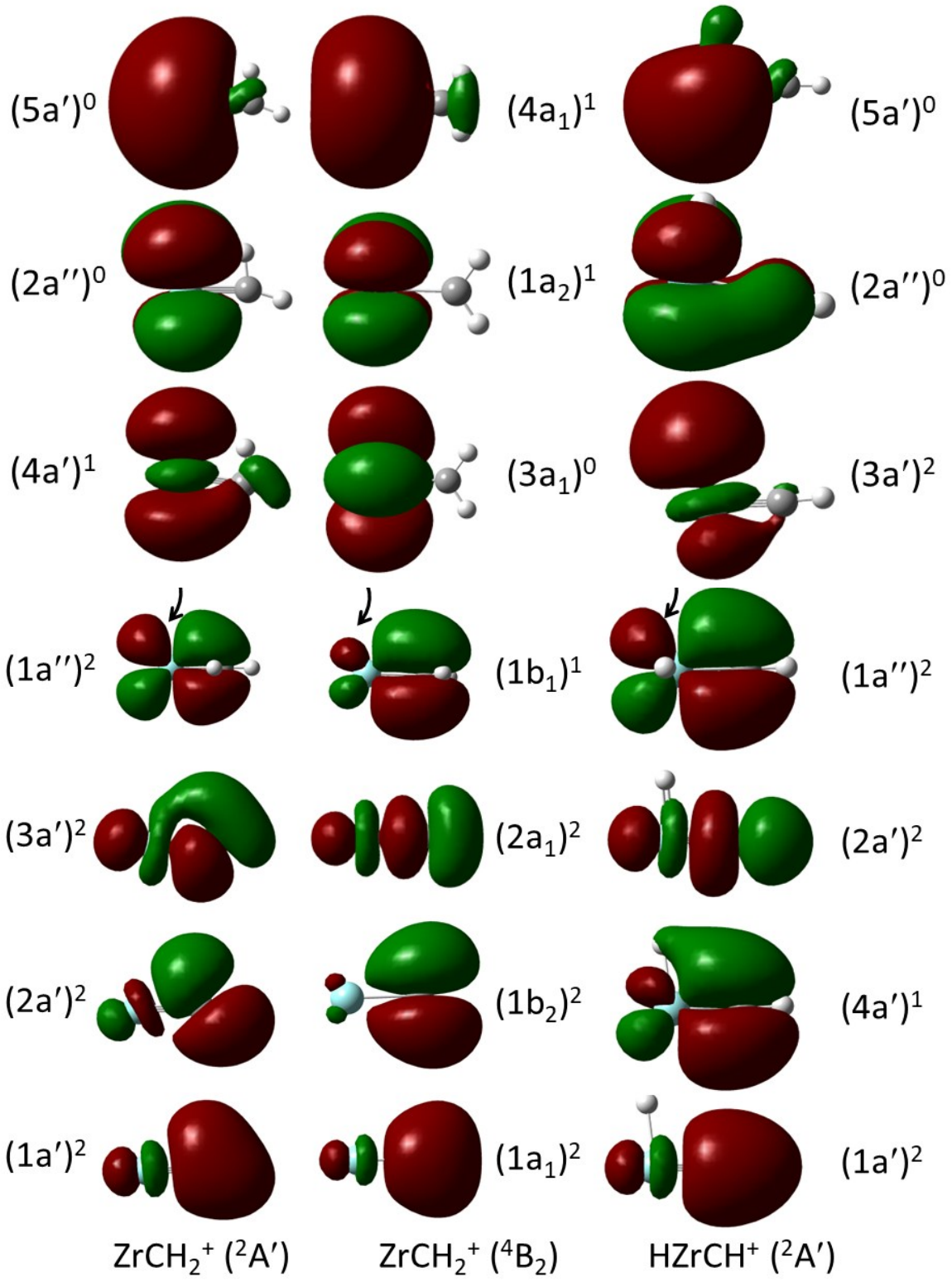

Figure 2: Molecular orbitals of several structures of $[Zr,C,2H]^+$. The molecule lies in the plane of the figure except for those marked by arrows, which are rotated 90° along the Zr–C bond axis.

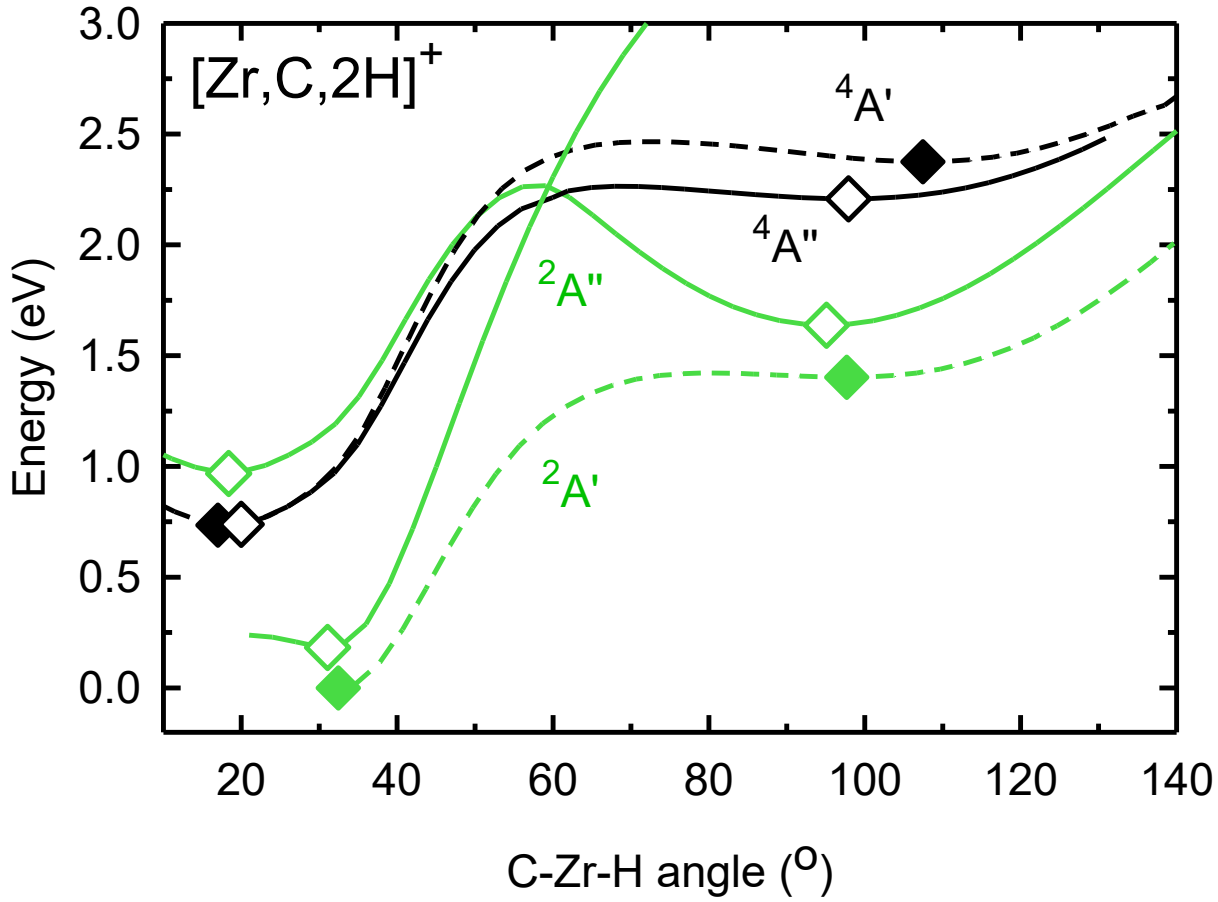

Figure 3: Potential energy surfaces of $[Zr,C,2H]^+$ along the C–Zr–H angle calculated at the uB3LYP/def2-TZVPPD level of theory. Diamonds indicate calculated structures that successfully converged to true minima at the indicated C–Zr–H angle. Solid lines indicate A" states while A' states are indicated by dashed lines. Doublet spin surfaces are depicted in green and quartet in black. All energy values are relative to the $^2A'$ GS structure.

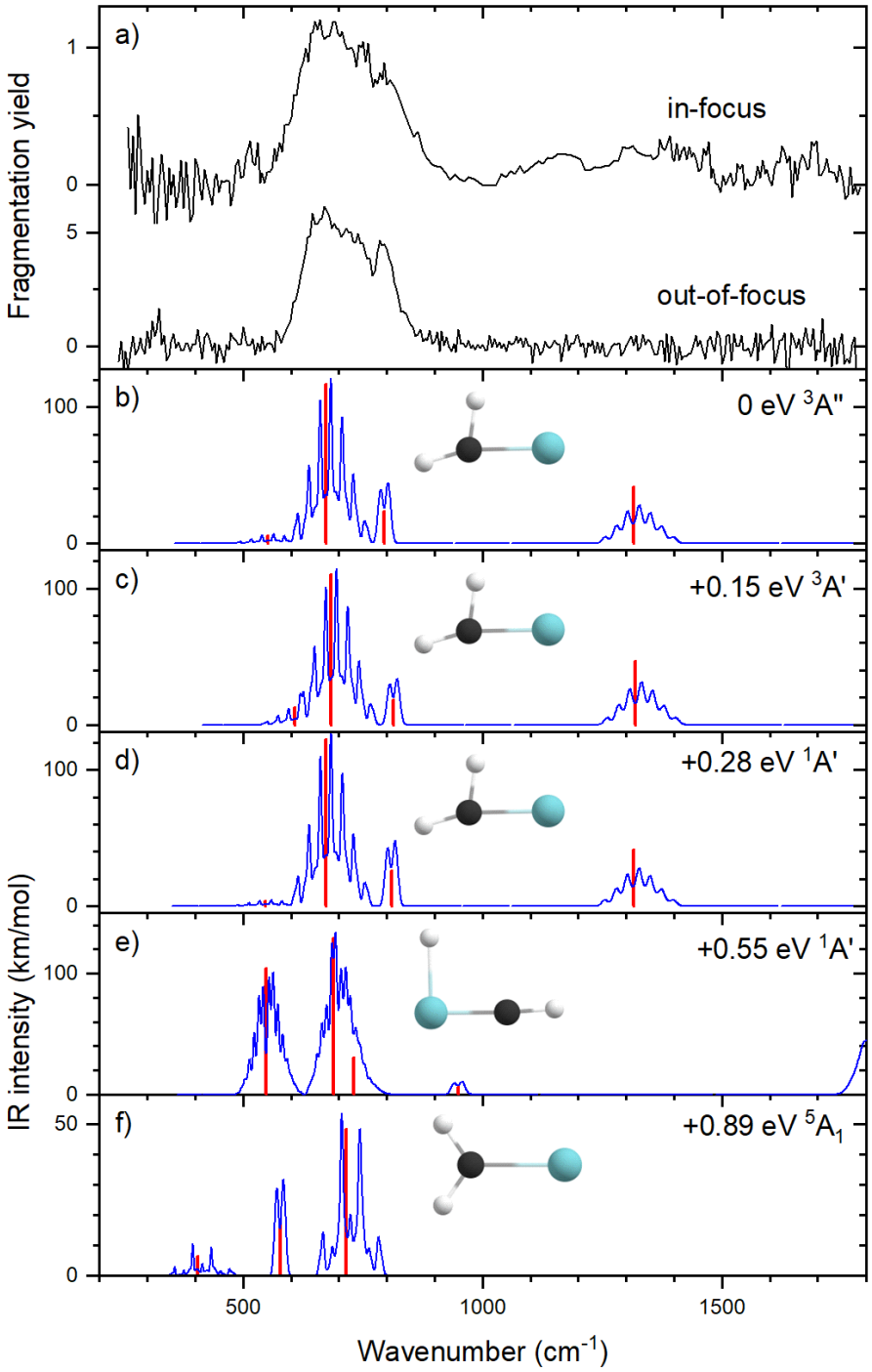

Figure 4: (a) Experimental IRMPD spectrum of $[Nb,C,2H]^+$; b-d) B3LYP/def2-TZVPPD calculated IR spectra of different $[Nb,C,2H]^+$ states and isomers with the harmonic vibrations in red and the rovibrational envelopes (calculated at 100 K) in blue accompanied by geometric structure, relative energy, and electronic state. Theoretical frequencies are scaled by 0.95.

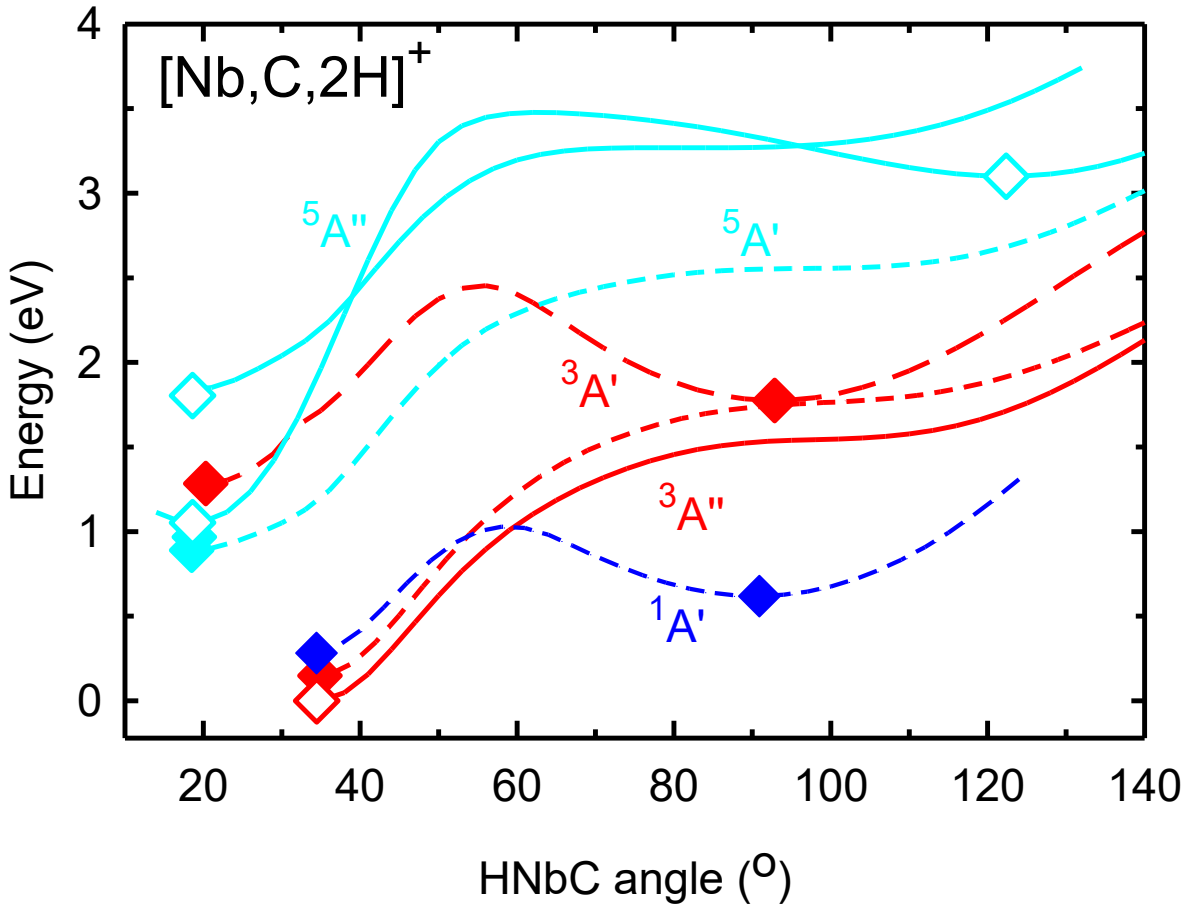

Figure 5: Potential energy surfaces of $[Nb,C,2H]^+$ along the C–Nb–H angle calculated at the uB3LYP/def2-TZVPPD level of theory. Diamonds indicate calculated structures that successfully converged to true minima at the indicated C–Nb–H angle. Solid lines indicate A″ states while A′ states are indicated by dashed lines. Singlet spin surfaces are depicted in blue, triplet in red, and quintet in cyan. All energy values are relative to the ^{3}A″ GS structure.